

Classification of Topological Phase Transitions and van Hove Singularity Steering Mechanism in Graphene Superlattices

Jian Wang¹ and Luiz H. Santos¹

¹*Department of Physics, Emory University, Atlanta, Georgia 30322, USA*

(Dated: December 7, 2020)

We study quantum phase transitions in graphene superlattices in external magnetic fields, where a framework is presented to classify multiflavor Dirac fermion critical points describing hopping-tuned topological phase transitions of integer and fractional Hofstadter-Chern insulators. We argue and provide numerical support for the existence of transitions that can be explained by a nontrivial interplay of Chern bands and van Hove singularities near charge neutrality. This work provides a route to critical phenomena beyond conventional quantum Hall plateau transitions.

Chern bands[1, 2] are the building blocks of the Hofstadter spectrum[3] when a large magnetic flux (of order $\phi_0 = h/e$) penetrates the unit cell of the 2D lattice. They give rise to quantum Hall phases beyond the Landau level (LL) paradigm, which has attracted considerable interest[4–8]. Rapid progress in the fabrication of superlattices with nanometer scale unit cells has led to the experimental realization of integer[9–12] and fractional[13] Hofstadter-Chern insulators (IHCI and FHCI), thereby opening remarkable prospects to explore the nontrivial interplay of lattice effects and electronic topology that is inaccessible in regular 2D lattices.

Topological ground states supported in Chern bands have been broadly studied using different approaches including numerical methods[4–8, 14–16], composite fermions[17–22] and Lieb-Schultz-Mattis type constraints.[23] On the other hand, the fundamental influence of lattice parameters on topological phase transitions (TPTs) in IHCI and FHCI has received significantly less attention.[24–26] The complexity of the Hofstadter spectrum and the finite bandwidth of Chern bands that reflects their dependence on the lattice parameters and on the intracell magnetic flux appears to stand in the way of an overarching understanding of lattice-tuned TPTs, which are distinct from plateau transitions tuned by the magnetic field.[27, 28]

In this Letter, we provide a classification of TPTs in IHCI and FHCI and present a mechanism for quantum criticality tuned by lattice parameters with a fixed background magnetic field. Numerical studies[24, 26] strongly support the existence of continuous TPTs tuned by the amplitude of a square lattice weak potential projected on the lowest LL. This work, on the other hand, employs an effective tight-binding description (i.e. “strong” potential) of a honeycomb superlattice with the magnetic field incorporated via Peierls substitution and discusses topological transitions tuned by hopping amplitudes of the lattice. Graphene superlattices realized via nanolithography [29–34] not only provide a motivation for this study but also offer promising test beds of these ideas.

The main results presented in this Letter are as follows: (1) We show that hopping-tuned TPTs on the hon-

eycomb lattice with a fixed rational intracell magnetic flux $\phi = (p/q)\phi_0$ are characterized by q Dirac fermions (DFs) located in high-symmetry momenta of the magnetic Brillouin zone. The number of DF flavors and their momentum space distribution are derived analytically from a nontrivial function that implicitly sets the momentum dependence of *all* the Chern bands of the spectrum. (2) We establish a surprising connection between van Hove singularities(VHSs)[35] and the onset of TPTs near charge neutrality. (3) This nonperturbative analysis is extended to hopping-tuned FHCI transitions described by composite fermions[17–22] in partially filled Chern bands.

Our setting is a honeycomb superlattice in a external perpendicular magnetic field, $B = \partial_x A_y - \partial_y A_x$, described by the single-particle nearest neighbor effective Hamiltonian

$$H = - \sum_{\langle \mathbf{r}, \mathbf{r}' \rangle} t_{\mathbf{r}, \mathbf{r}'} e^{i \frac{2\pi}{\phi_0} \int_{\mathbf{r}}^{\mathbf{r}'} d\mathbf{x} \cdot \mathbf{A}(\mathbf{x})} a_{\mathbf{r}}^\dagger b_{\mathbf{r}'} + \text{H.c.} \quad (1)$$

$a_{\mathbf{r}}^\dagger = a_{m,n}^\dagger$ and $b_{\mathbf{r}}^\dagger = b_{m,n}^\dagger$ are spin polarized fermionic creation operators on the two sublattices, $\mathbf{r} = m\mathbf{a}_1 + n\mathbf{a}_2$, $m, n \in \mathbb{Z}$ is the lattice vector with basis vectors $\mathbf{a}_1 = a(3/2, -\sqrt{3}/2)$ and $\mathbf{a}_2 = a(3/2, \sqrt{3}/2)$, and $t_{\mathbf{r}, \mathbf{r}'} = \{t_1, t_2, t_3\}$ are nearest neighbor real hopping elements, as shown in (a) in Fig.1.

Working in the gauge $\mathbf{A} = \hat{y}(x + \sqrt{3}y)B$ with rational flux $\phi = B \frac{\sqrt{3}}{2} a^2 = (p/q)\phi_0$ ($p, q \in \mathbb{Z}_+$ and coprime), we introduce the magnetic unit cell containing $2q$ sites as in Fig.1(a), which leads to the \mathbf{k} -space Hamiltonian [36] $H = - \sum_{\mathbf{k} \in \text{MBZ}} \psi_{\mathbf{k}}^\dagger \tau_1 \otimes h_{\mathbf{k}} \psi_{\mathbf{k}}$, where $\mathbf{k} = (k_1, k_2) \equiv k_1 \hat{\mathbf{g}}_1 + k_2 \hat{\mathbf{g}}_2$ is the momentum expanded along the reciprocal lattice vectors $\hat{\mathbf{g}}_{1,2}$.

Aiming at a nonperturbative description of the Chern bands beyond the isotropic lattice $t_1 = t_2 = t_3$ [37–39], we establish the spectral function $\mathcal{P}(E) = \det(EI - H)$,

$$\mathcal{P}(E) = \sum_{n=1}^q a_n(\{t_i\}) E^{2n} - \xi^2(\{t_i\}, k_1, k_2), \quad (2a)$$

$$\xi(\{t_i\}, k_1, k_2) = |t_1^q e^{iqk_1 - i\pi(q-1)} + t_2^q e^{ik_2} + t_3^q| \geq 0. \quad (2b)$$

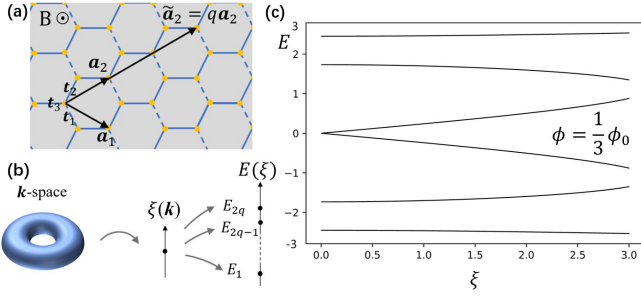


FIG. 1. Parameterization of the Hofstadter-Chern bands by the Thouless function. (a) Honeycomb superlattice with lattice constant a in the nanometers and magnetic unit cell q times extended along \mathbf{a}_2 . (b) Momentum dependence on the Thouless function ξ . (c) Spectrum as function of ξ for $\phi = (1/3)\phi_0$.

Equation (2) encodes a remarkable property of the Hofstadter spectrum [originally noticed by Thouless in a different context[40] (see also[37])], namely, that the momentum dependence of the bands is “compressed” in a single function $\xi(\mathbf{k})$, i.e. $E_\alpha(\mathbf{k}) = E_\alpha[\xi(\mathbf{k})]$ for $\alpha = 1, \dots, 2q$. Figure. 1(b), (c) shows how the energy bands depend on the “Thouless function” ξ , which we notice is related to the graphene band [41] upon the replacements $(k_1, k_2) \rightarrow [qk_1 - \pi(q-1), k_2]$ and $\{t_i\} \rightarrow \{t_i^q\}$.

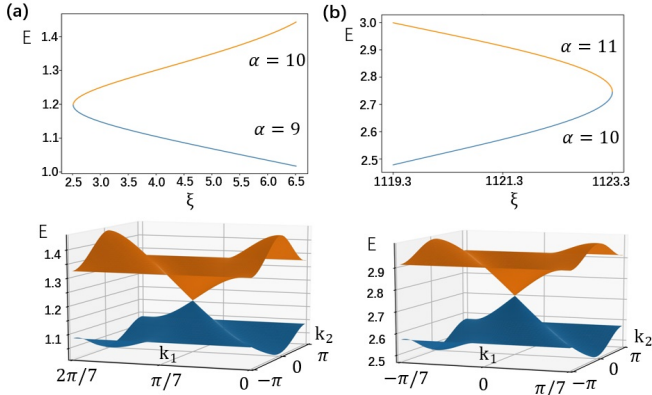


FIG. 2. TPTs of the $\phi = (1/7)\phi_0$ lattice (α denotes band index). (a) At $(t_1, t_2, t_3) = (1.24, 1, 1)$, 7 Dirac cones (only one shown) form at $\mathbf{k}_{min}^{(n)} = (-\pi/7 + 2\pi n/7, 0)$, $n = 0, \dots, 6$. (b) At $(t_1, t_2, t_3) = (2.73, 1, 1)$, 7 Dirac cones (only one shown) form at $\mathbf{k}_{max}^{(n)} = (2\pi n/7, 0)$, $n = 0, \dots, 6$.

IHCI transitions - We now establish a classification of TPTs in the parameter space (t_1, t_2, t_3) . On general grounds, consider a TPT tuned by the hopping parameters where two Chern bands touch at (ξ_F, E_F) , where $\xi_F \neq 0$ and $E_F \neq 0$ is the Fermi energy. ($(\xi_F = 0, E_F = 0)$ band touchings will be discussed shortly after.) Let $\mathcal{P}(E) = \sum_{n=1}^q c_n (E^2 - E_F^2)^n - (\xi^2 - \xi_F^2)$ be the Taylor expansion of the characteristic polynomial Eq.(2a) about the band touching point. The even

powers of E in Eq.(2a) reflect the spectral particle-hole symmetry, and, since $\pm E_F \neq 0$ are doubly degenerate roots of the characteristic polynomial, it follows that $\mathcal{P}(E) = (E^2 - E_F^2)^2 g(E)$, where $g(E)$ is a polynomial in E of order $2(q-2)$. This readily implies the coefficient $c_1 = 0$, leading to the relation in the vicinity of the touching point,

$$\xi \approx \xi_F + 2c_2 E_F^2 \xi_F^{-1} (E - E_F)^2, \quad \xi_F \neq 0. \quad (3)$$

Consequently, the sign of c_2 determines whether the transition occurs through the quadratic minimum ($\xi_F = \xi_{min} > 0$) or maximum ($\xi_F = \xi_{max} > 0$) of the Thouless function. Furthermore, upon expanding near the extremal points, i.e., $\xi(\mathbf{k}) \approx \xi_{min(max)} + \frac{a}{2} (\mathbf{k} - \mathbf{k}_{min(max)})^2$ [with $a > 0 (< 0)$ being the nonzero curvature at the quadratic minima (maxima)], and substituting onto Eq.(3), we obtain the dispersion

$$E - E_F = \pm v_F^* |\mathbf{k} - \mathbf{k}_{min(max)}|, \quad v_F^* = (a\xi_F/4c_2 E_F^2)^{1/2}, \quad (4)$$

characteristic of a Dirac cone centered at $\mathbf{k}_{min(max)}$. It can be shown that higher order band touchings are forbidden. Importantly, we establish below that ξ has q minima and maxima, implying a q -component Dirac transition. Figure 2 presents two IHCI TPTs for $\phi = \phi_0/7$ that confirm the general behavior described in Eq.(3) and Eq.(4). The considerations above, therefore, uncover a nontrivial link between the classification of critical points and the global properties of the Thouless function, which we now address in detail.

Eq.(2a) establishes a one-to-one correspondence between the zero modes of ξ and band touchings at $E = 0$, where $E \approx \pm \xi/a_1^{1/2}$. Then, we directly determine from Eq.(2b) that the band structure with isotropic hoppings supports $2q$ Dirac touchings at $E = 0$ [42–44] located at

$$\mathbf{K}_{\pm}^{(n)} = \left[\pm \frac{2\pi}{3q} + \frac{\pi}{q} (2n + q - 1), \mp \frac{2\pi}{3} \right], \quad (5)$$

for $n = 0, \dots, q-1$, and, furthermore, that these band touchings persist as long as

$$\left| |t_i|^q - |t_j|^q \right| \leq |t_k|^q \leq \left| |t_i|^q + |t_j|^q \right| \quad (6)$$

where i, j, k are identified with any of the distinct values of $1, 2, 3$. Equation (6) is the condition for $\xi = 0$, which, reproduces the stability of the pair of Dirac cones in graphene bands when $q = 1$. [45, 46] The global properties of the Thouless function lead to a remarkably simple classification of critical points:

(1) When the equation (6) condition holds, $\xi \geq 0$ and there are $2q$ Dirac band touchings at $(\xi = 0, E = 0)$ as a consequence of particle-hole symmetry. Furthermore, TPTs at nonzero Fermi energy occur through q Dirac band touchings located at $\mathbf{k}_{max}^{(n)} = [\pi(2n + q - 1)/q, 0]$, $n = 0, \dots, q-1$, where $\xi[\mathbf{k}_{max}^{(n)}] = \xi_{max}$. However,

$\xi = \xi_{min} = 0$ transitions are forbidden at $E \neq 0$ by particle-hole symmetry[36].

(2) Outside the parameter space (6), $\xi > 0$ and the spectrum has a gap at half filling. The $2q$ zero modes of ξ merge pairwise forming q quadratic minima at one of the saddle points $\mathbf{M}_1^{(n)} = [\pi(2n + q - 1)/q, -\pi]$, $\mathbf{M}_2^{(n)} = [-\pi/q + \pi(2n + q - 1)/q, 0]$ or $\mathbf{M}_3^{(n)} = [-\pi/q + \pi(2n + q - 1)/q, -\pi]$, for $n = 0, \dots, q - 1$. Then, $E_F \neq 0$ critical points are realized by q Dirac band touchings located either at ξ_{min} or ξ_{max} . Taking, for concreteness,

$$t_2 = t_3 = 1, \quad t_1 > 0, \quad (7)$$

leads to case (1) for $0 < t_1 \leq 2^{1/q}$ and case (2) when $t_1 > 2^{1/q}$, where the q degenerate minima of ξ are located at $\mathbf{k}_{min}^{(n)} = \mathbf{M}_2^{(n)}$, for $n = 0, \dots, q - 1$. The TPTs of Fig.(2) correspond to case (2) with the hopping parameters Eq.(7).

(3) The q Dirac fermions at quantum criticality are constrained by the action of magnetic translation, under which $(k_1, k_2) \rightarrow (k_1 + \frac{2\pi}{q}, k_2)$, and they account for the transfer of Chern number $\Delta C = \pm q$ between the bands, according to standard parity anomaly considerations.[47] We have performed extensive numerical calculations that confirm the properties (1), (2) and (3).

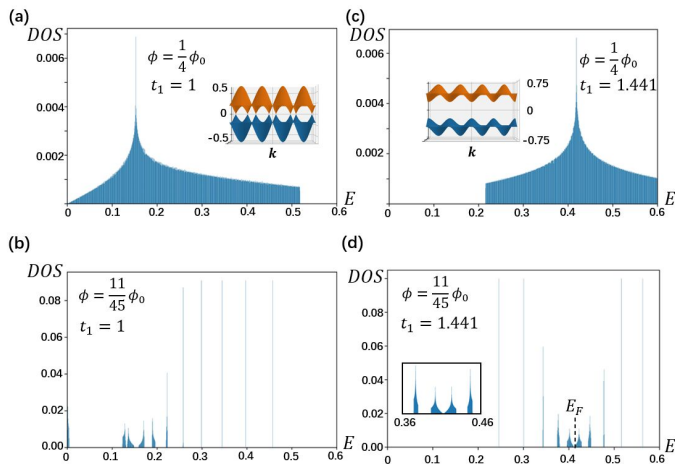


FIG. 3. Comparison between the density of states of system A and B. (a) DOS of the Dirac center band at $\phi_A = (1/4)\phi_0$ and $(t_1, t_2, t_3) = (1, 1, 1)$. Inset: eight gapless DFs with locations given by Eq.(5). (b) DOS at $\phi_B = (11/45)\phi_0$ and $(t_1, t_2, t_3) = (1, 1, 1)$ reflecting the reconstruction of the Dirac band in (a). (c) DOS of the Dirac center band at $\phi_A = (1/4)\phi_0$ and $(t_1, t_2, t_3) = (1.441, 1, 1)$. Inset: eight gapped DFs with the gap-opening threshold $t_1 = 2^{1/4} \approx 1.19$. (d) DOS at $\phi_B = (11/45)\phi_0$ and $(t_1, t_2, t_3) = (1.441, 1, 1)$ reflecting the reconstruction of the gapped Dirac band in (c). Inset shows emergent Dirac fermions at the critical point.

Having classified the IHCI critical points, we now address the *mechanism* underlying such phenomena, which must account for $\Delta C = \pm q$ transitions in a spectrum composed primarily of bands which $C \sim O(1)$. Re-

markably, we argue and numerically demonstrate that $\Delta C = \pm q$ TPTs occur when Chern bands cross the energy scales associated with the VHS of the DF band close to charge neutrality. In what follows, we shall demonstrate this striking phenomenon using the hopping t_1 in Eq.(7) as the tuning parameter.

To unearth the connection between VHSs and TPTs, we consider two Hofstadter systems, denoted A and B, with fluxes $\phi_A = p_A/q_A$ and $\phi_B = p_B/q_B$ [henceforth we set $h = e = 1$ such that $\phi_0 = 1$ and $\phi \sim \phi \pmod{1}$]. Furthermore, we impose the conditions (a) $|(\phi_A - \phi_B)/\phi_0| \ll 1$ and (b) $q_B \gg q_A$, which associate the spectrum of B with subbands of the A system that arise due to a small residual flux. By this construction, the B bands away from the VHS energy E_{VHS}^A behave as pseudo-LLs (pLL) of the A system with $C_{pLL} \sim O(1)$. Consequently, we argue, and numerically confirm, that E_{VHS}^A provides the natural energy scale supporting nontrivial VHS-Chern bands of B with $C_{VHS} \sim O(q_B)$. Therefore, the dependence of E_{VHS}^A on hopping parameters reveals the location of the nontrivial TPTs of B characterized by $\Delta C = \pm q_B$.

To gain further insight on the relation between VHSs and TPTs, we initially consider system A with $t_i = 1$, which displays $2q_A$ DFs at half filling with $E_{Dirac}^A(\mathbf{k}) \approx \xi_A(t_i = 1; \mathbf{k} - \mathbf{K}_{\pm})/a_1^{1/2}$; see Eq.(5). Due to particle-hole symmetry, we focus on $E \geq 0$ bands. General considerations give the Dirac-like density of states (DOS) $D_A \propto E$ near charge neutrality, which is cut off by the VHS energy E_{VHS}^A that distinguishes the electronlike states from the holelike states. Figure 3(a) displays the DOS of this band for $\phi_A = 1/4$, which supports eight Dirac fermions and has $E_{VHS}^A \approx 0.15$. Notice that, compared to the graphene bands[41], the magnetic field pushes the VHS substantially closer to charge neutrality due to the splitting of the spectrum into $2q_A$ bands. Furthermore, conditions (a) and (b) ensure the spectrum of B near half filling can be understood as the response of the DF band of A to a weak “residual” magnetic field, which is expected to give rise to relativisticlike (nonrelativistic-like) LLs for $E \lesssim (\gtrsim)E_{VHS}^A$. However, the B bands close to E_{VHS}^A deviate substantially from the LL behavior, confirming the behavior described in the paragraph above. This is illustrated in Fig.3(b) where the said bands of the $\phi_B = 11/45$ system show more pronounced bandwidths and narrower gaps.

To understand how E_{VHS}^A tracks the TPTs of the B system, we study the dependence of Thouless function on the hopping parameters. The property $E_{\alpha}(\mathbf{k}) = E_{\alpha}[\xi(\mathbf{k})]$ establishes that the VHSs of the Chern bands are located on the saddles of ξ . Direct calculation shows that ξ is degenerate on all the saddle points $\mathbf{M}_{1,2,3}^{(n)}$ when $t_1 = 1$ and, furthermore, that the degeneracy is partially broken for $t_1 \neq 1$. [36] For $1 < t_1 < 2^{1/q}$ [case (1) above], the VHS splits into a large peak at $E_{VHS,1}^A \equiv E^A[\mathbf{M}_1^{(n)}]$

and a small peak at $E_{\text{VHS},2}^A \equiv E^A(M_2^{(n)})$. The latter disappears in the lower band edge, for $t_1 > 2^{1/q}$ [case (2) above], where an energy gap forms [Fig. 3(c)]. Moreover, Fig. 3(d) (see inset) displays the onset of a TPT as the result of the VHS-Chern bands being steered by the $E_{\text{VHS},1}^A$ energy scale.

The striking relationship between VHS and TPTs is shown in Fig. 4, where the bands of the $\phi_B = p_B/q_B = 11/45$ system near charge neutrality are plotted in the interval $t_1 \geq 1$. These bands originate as subbands of the $\phi_A = p_A/q_A = 1/4$ Dirac band in response to a small flux deviation $\delta\phi = -1/180$, as per conditions (a) and (b). We observe that the B bands formed near the band edges of system A behave as pLLs with vanishing bandwidth and $C_{\text{pLL}} = -4$, while the VHS-Chern bands carrying $C_{\text{VHS}} \sim O(q_B)$ form in the vicinity of E_{VHS}^A . Because E_{VHS}^A changes with the hopping parameters, the change in t_1 away from the isotropic point steers the VHS-Chern bands of B along the solid green ($E_{\text{VHS},1}^A$) and purple ($E_{\text{VHS},2}^A$) lines. This VHS steering mechanism reveals a sequence of TPTs (up arrows) characterized by $\Delta C = \pm 45$, with 45 emerging DFs located at the extremum points of the Thouless function of the system B, confirming the general properties (1), (2) and (3). For results on other flux states, see the Supplemental Material[36].

FHCI transitions – Our analysis can be further extended to describe FHCI transitions tuned by the hopping parameters in partially filled Chern bands. via the standard representation of an FHCI with Hall conductance $\sigma_{xy}(C) = C/(2C + 1)$ in terms of a composite fermion system [17, 18, 48] in an IHCI with $\sigma_{xy}^{CF} = C[19, 20]$, which is subject to a mean field residual flux

$$\phi_{CF} = \phi - \phi_{CS}, \quad (8)$$

where $\phi = B \frac{\sqrt{3}}{2} a^2$ and $\phi_{CS} = 4n$ (the factor of 4 accounts for two attached flux quanta and two sites per unit cell) are, respectively, the intracell fluxes due to the external magnetic field and the Chern-Simons gauge field at lattice filling n , for $0 \leq n \leq 1$. Then, a TPT at fixed B and n between FHCIs with $\sigma_{xy}(C_1) = C_1/(2C_1 + 1)$ and $\sigma_{xy}(C_2) = C_2/(2C_2 + 1)$ can be effectively described by a $C_1 \rightarrow C_2$ composite fermion transition subject to the constraint $|C_2 - C_1| = q_{cf}$ (recall property (3)), where $\phi_{CF} = p_{cf}/q_{cf}$ is the flux of the composite fermion state. Furthermore, the relationship Eq.(8) between B and n allows the identification of candidate TPTs between Abelian FHCI states. In closing we present two such FHCI transitions realized when $\phi_{CF} = 11/45$, which are shown by vertical red arrows in Fig. 4. The first TPT is observed at ($t_1 \approx 1.02, n = 47/9, \phi = 1/3$) and represents a transition between FHCIs with $\sigma_{xy}(37) = 37/75$ and $\sigma_{xy}(-8) = 8/15$. On the second transition at ($t_1 \approx 1.44, n = 50/90 = 5/9, \phi = 7/15$), the Hall conductance jumps from $\sigma_{xy}(25) = 25/51$ to $\sigma_{xy}(-20) = 20/39$.

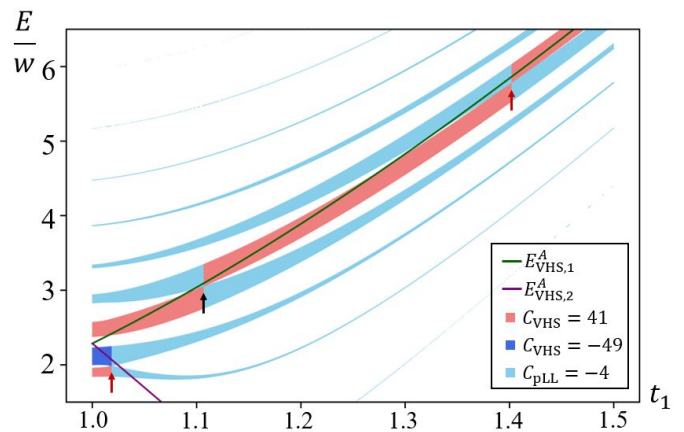


FIG. 4. TPTs of system B ($\phi_B = 11/45$) steered by the VHSs of system A ($\phi_A = 1/4$). Eleven B bands form near charge neutrality by splitting of the Dirac band of A in response to a flux deviation $\delta\phi = -1/180$, where nine of these bands are shown. All energies are rescaled by the average band separation w of the B system with $t_1 = 1$. The Chern numbers of the bands are indicated by color coding. $E_{\text{VHS},1}^A$ and $E_{\text{VHS},2}^A$ are represented, respectively, by solid green and purple lines. The composite fermion (IHCI) TPTs at $n = 47/90$ and $n = 50/90$ ($n = 49/90$) are marked by vertical red (black) arrows.

We point the reader to the Supplemental Material [36] for another example of FHCI transition.

In summary, we have proposed an analytical framework to classify multiflavor Dirac fermion critical points describing hopping-tuned TPTs of integer and fractional Hofstadter-Chern insulators in honeycomb superlattices. Our classification sets firm constraints on the number of Dirac flavors as well as their momentum space distribution in terms of the hopping parameters, the magnetic flux per unit cell and the electron density. Such critical points realize large transfers of Chern number across the TPT, which can be detected via conductivity measurements. We have identified a series of TPTs that can be explained by the nontrivial response of Chern bands to VHSs near charge neutrality. These results, which were derived from the identification of global properties of the Chern bands, lead to a new understanding of quantum critical phenomena resulting from the interplay of magnetic fields and VHSs. This work opens many interesting directions to study quantum critical phenomena in superlattices. Besides nanopatterned graphene superlattices [29–34] that served as a motivation for this work, van der Waals heterostructures in external magnetic field[9–11, 13] provide promising platforms to realize topological quantum criticality via strain induced tuning of the effective hopping parameters. Also, the interplay of magnetic fields and higher order VHSs[49, 50] can potentially provide even richer critical phenomena. We leave these open questions to future work.

We thank Claudio Chamon, Ankur Das, Ribhu Kaul, Ganpathy Murthy and Raman Sohal for useful discus-

sions. Part of this work was performed at the Aspen Center for Physics, which is supported by National Science Foundation Grant No. PHY-1607611. L. H. S. is supported by a faculty startup at Emory University.

Note added in proof—Recently, we became aware of a related work, Ref.[51], which studies quantum phase transitions in Hofstadter bands by tuning the magnetic flux per unit cell.

-
- [1] D. J. Thouless, M. Kohmoto, M. P. Nightingale, and M. den Nijs, Phys. Rev. Lett. **49**, 405 (1982).
- [2] F. D. M. Haldane, Phys. Rev. Lett. **61**, 2015 (1988).
- [3] D. R. Hofstadter, Phys. Rev. B **14**, 2239 (1976).
- [4] T. Neupert, L. Santos, C. Chamon, and C. Mudry, Phys. Rev. Lett. **106**, 236804 (2011).
- [5] D. N. Sheng, Z.-C. Gu, K. Sun, and L. Sheng, Nature Communications **2**, 389 EP (2011).
- [6] E. Tang, J.-W. Mei, and X.-G. Wen, Phys. Rev. Lett. **106**, 236802 (2011).
- [7] K. Sun, Z. Gu, H. Katsura, and S. Das Sarma, Phys. Rev. Lett. **106**, 236803 (2011).
- [8] N. Regnault and B. A. Bernevig, Phys. Rev. X **1**, 021014 (2011).
- [9] C. R. Dean, L. Wang, P. Maher, C. Forsythe, F. Ghahari, Y. Gao, J. Katoch, M. Ishigami, P. Moon, M. Koshino, T. Taniguchi, K. Watanabe, K. L. Shepard, J. Hone, and P. Kim, Nature **497**, 598 EP (2013).
- [10] L. A. Ponomarenko, R. V. Gorbachev, G. L. Yu, D. C. Elias, R. Jalil, A. A. Patel, A. Mishchenko, A. S. Mayorov, C. R. Woods, J. R. Wallbank, M. Mucha-Kruczynski, B. A. Piot, M. Potemski, I. V. Grigorieva, K. S. Novoselov, F. Guinea, V. I. Fal'ko, and A. K. Geim, Nature **497**, 594 EP (2013).
- [11] B. Hunt, J. D. Sanchez-Yamagishi, A. F. Young, M. Yankowitz, B. J. LeRoy, K. Watanabe, T. Taniguchi, P. Moon, M. Koshino, P. Jarillo-Herrero, and R. C. Ashoori, Science **340**, 1427 (2013).
- [12] C. Forsythe, X. Zhou, K. Watanabe, T. Taniguchi, A. Papathevas, P. Moon, M. Koshino, P. Kim, and C. R. Dean, Nature nanotechnology **13**, 566 (2018).
- [13] E. M. Spanton, A. A. Zibrov, H. Zhou, T. Taniguchi, K. Watanabe, M. P. Zaletel, and A. F. Young, Science **360**, 62 (2018).
- [14] Z. Liu, E. J. Bergholtz, H. Fan, and A. M. Läuchli, Phys. Rev. Lett. **109**, 186805 (2012).
- [15] Y.-L. Wu, B. A. Bernevig, and N. Regnault, Phys. Rev. B **85**, 075116 (2012).
- [16] A. M. Läuchli, Z. Liu, E. J. Bergholtz, and R. Moessner, Phys. Rev. Lett. **111**, 126802 (2013).
- [17] J. K. Jain, Phys. Rev. Lett. **63**, 199 (1989).
- [18] A. López and E. Fradkin, Phys. Rev. B **44**, 5246 (1991).
- [19] A. Kol and N. Read, Phys. Rev. B **48**, 8890 (1993).
- [20] G. Möller and N. R. Cooper, Phys. Rev. Lett. **115**, 126401 (2015).
- [21] G. Murthy and R. Shankar, Phys. Rev. B **86**, 195146 (2012).
- [22] R. Sohal, L. H. Santos, and E. Fradkin, Phys. Rev. B **97**, 125131 (2018).
- [23] Y.-M. Lu, Y. Ran, and M. Oshikawa, Annals of Physics **413**, 168060 (2020).
- [24] D. Pfannkuche and A. H. MacDonald, Physical Review B **56**, R7100 (1997).
- [25] M. Sato, D. Tobe, and M. Kohmoto, Phys. Rev. B **78**, 235322 (2008).
- [26] J. Y. Lee, C. Wang, M. P. Zaletel, A. Vishwanath, and Y.-C. He, Phys. Rev. X **8**, 031015 (2018).
- [27] J. K. Jain, S. A. Kivelson, and N. Trivedi, Phys. Rev. Lett. **64**, 1297 (1990).
- [28] S. Kivelson, D.-H. Lee, and S.-C. Zhang, Phys. Rev. B **46**, 2223 (1992).
- [29] M. Gibertini, A. Singha, V. Pellegrini, M. Polini, G. Vignale, A. Pinczuk, L. N. Pfeiffer, and K. W. West, Phys. Rev. B **79**, 241406 (2009).
- [30] A. Singha, M. Gibertini, B. Karmakar, S. Yuan, M. Polini, G. Vignale, M. I. Katsnelson, A. Pinczuk, L. N. Pfeiffer, K. W. West, and V. Pellegrini, Science **332**, 1176 (2011).
- [31] A. Soibel, U. Meirav, D. Mahalu, and H. Shtrikman, Semiconductor Science and Technology **11**, 1756 (1996).
- [32] L. Nádvořník, M. Orlita, N. A. Goncharuk, L. Smrčka, V. Novák, V. Jurka, K. Hruška, Z. Výborný, Z. R. Wasilewski, M. Potemski, and K. Výborný, New Journal of Physics **14**, 053002 (2012).
- [33] S. Wang, D. Scarabelli, Y. Y. Kuznetsova, S. J. Wind, A. Pinczuk, V. Pellegrini, M. J. Manfra, G. C. Gardner, L. N. Pfeiffer, and K. W. West, Applied Physics Letters **109**, 113101 (2016).
- [34] S. Wang, D. Scarabelli, L. Du, Y. Y. Kuznetsova, L. N. Pfeiffer, K. W. West, G. C. Gardner, M. J. Manfra, V. Pellegrini, S. J. Wind, and A. Pinczuk, Nature Nanotechnology **13**, 29 (2018).
- [35] L. Van Hove, Phys. Rev. **89**, 1189 (1953).
- [36] See Supplemental Material for details on further examples of the relation between the vHs energy scale and topological phase transitions.
- [37] R. Rammal, Journal de Physique **46**, 1345 (1985).
- [38] B. Andrei Bernevig, T. L. Hughes, S.-c. Zhang, H.-d. Chen, and C. Wu, International Journal of Modern Physics B **20**, 3257 (2006).
- [39] A. Agazzi, J.-P. Eckmann, and G. M. Graf, Journal of Statistical Physics **156**, 417 (2014).
- [40] D. J. Thouless, Phys. Rev. B **28**, 4272 (1983).
- [41] A. H. Castro Neto, F. Guinea, N. M. R. Peres, K. S. Novoselov, and A. K. Geim, Rev. Mod. Phys. **81**, 109 (2009).
- [42] J.-W. Rhim and K. Park, Phys. Rev. B **86**, 235411 (2012).
- [43] I. N. Karnaukhov, Physics Letters A **383**, 2114 (2019).
- [44] A. Das, R. K. Kaul, and G. Murthy, Phys. Rev. B **101**, 165416 (2020).
- [45] Y. Hasegawa, R. Konno, H. Nakano, and M. Kohmoto, Phys. Rev. B **74**, 033413 (2006).
- [46] B. Wunsch, F. Guinea, and F. Sols, New Journal of Physics **10**, 103027 (2008).
- [47] A. N. Redlich, Phys. Rev. Lett. **52**, 18 (1984).
- [48] B. I. Halperin, P. A. Lee, and N. Read, Phys. Rev. B **47**, 7312 (1993).
- [49] D. V. Efremov, A. Shtyk, A. W. Rost, C. Chamon, A. P. Mackenzie, and J. J. Betouras, Physical Review Letters **123**, 207202 (2019).
- [50] N. F. Q. Yuan, H. Isobe, and L. Fu, Nature Communications **10**, 5769 (2019).
- [51] J. Herzog-Arbeitman, Z.-D. Song, N. Regnault, and

Supplemental Material

HONEYCOMB HOFSTADTER HAMILTONIAN IN THE MOMENTUM SPACE

In this section we provide details of the momentum space form of the Hamiltonian, which was omitted in the main text. In the gauge $\mathbf{A} = \hat{y}(x + \sqrt{3}y)B$, the real space Hamiltonian

$$H = - \sum_{\langle r, r' \rangle} t_{r, r'} e^{i \frac{2\pi}{\phi_0} \int_r^{r'} dx \cdot \mathbf{A}(x)} a_r^\dagger b_{r'} + \text{H.c.} \quad (\text{S1})$$

takes the form

$$H = - \sum_{m, n} a_{m, n}^\dagger \left(t_3 + \omega^{-n} t_1 \hat{T}_{\mathbf{a}_1} + \omega^n t_2 \hat{T}_{\mathbf{a}_2} \right) b_{m, n} + \text{H.c.} \quad (\text{S2})$$

where $t_{1,2,3}$ are nearest neighbor real hopping elements shown in Fig.(1a) of the main text, $\omega = e^{2\pi i \frac{p}{q}}$ and $\hat{T}_{\mathbf{a}_{1,2}}$ are the translation operators on the $\mathbf{a}_{1,2}$ directions, with the lattice constant $a = 1$. The magnetic unit cell is formed by extending the original one q times in the \mathbf{a}_2 direction (see Fig.(1a) of the main text), giving rise to an effective tight-binding description with $2q$ sites per magnetic unit cell, (a_r^s, b_r^s) , where $s = 0, \dots, q-1$, and translation vectors $\{\tilde{\mathbf{a}}_1, \tilde{\mathbf{a}}_2\} = \{\mathbf{a}_1, q \mathbf{a}_2\}$. Then in momentum space, we readily find

$$H = - \sum_{\mathbf{k} \in \text{MBZ}} \psi_{\mathbf{k}}^\dagger \begin{pmatrix} 0 & h_{\mathbf{k}} \\ h_{\mathbf{k}}^\dagger & 0 \end{pmatrix} \psi_{\mathbf{k}} = - \sum_{\mathbf{k} \in \text{MBZ}} \psi_{\mathbf{k}}^\dagger \tau_1 \otimes h_{\mathbf{k}} \psi_{\mathbf{k}}, \quad (\text{S3})$$

with nonzero matrix elements of the $q \times q$ matrix $h_{\mathbf{k}}$ given by

$$\begin{aligned} (h_{\mathbf{k}})_{ss} &= t_3 + t_1 e^{ik_1} \omega^{-s}, \quad s = 0, \dots, q-1, \\ (h_{\mathbf{k}})_{s, s+1} &= t_2 \omega^s, \quad s = 0, \dots, q-2, \\ (h_{\mathbf{k}})_{q-1, 0} &= t_2 \omega^{q-1} e^{ik_2}, \end{aligned} \quad (\text{S4})$$

where $\mathbf{k} = k_1 \tilde{\mathbf{g}}_1 + k_2 \tilde{\mathbf{g}}_2$, with $k_i \in [-\pi, \pi)$, denotes the momenta inside the magnetic Brillouin zone (MBZ) with $\tilde{\mathbf{g}}_1 = \frac{1}{3}\hat{x} - \frac{1}{\sqrt{3}}\hat{y}$ and $\tilde{\mathbf{g}}_2 = \frac{1}{q}(\frac{1}{3}\hat{x} + \frac{1}{\sqrt{3}}\hat{y})$ being the reciprocal vectors in Cartesian coordinates satisfying $\tilde{\mathbf{a}}_i \cdot \tilde{\mathbf{g}}_j = \delta_{ij}$.

We now provide an explicit proof that the momentum dependence of the characteristic polynomial appears only in the $a_0 = -\xi^2 = (-1)^{q-1} \det(H)$ coefficient. By examining the matrix elements given in (S4), we notice that the dependence on k_2 appears only in $(H_{\mathbf{k}})_{q-1, q} = (h_{\mathbf{k}})_{q-1, 0}$ and $(H_{\mathbf{k}})_{q, q-1} = (h_{\mathbf{k}}^\dagger)_{0, q-1}$. As such, these two elements only contribute to the coefficient $a_0 = -\xi^2 = (-1)^{q-1} \det(H)$ of the characteristic polynomial (2a):

$$\begin{aligned} a_0 &= (-1)^{q-1} \det(H) \\ &= - \prod_{s=0}^{q-1} |t_3 + t_1 \omega^s e^{-ik_1}|^2 - |e^{ik_2} \prod_{s=0}^{q-1} t_2 \omega^s|^2 - (e^{ik_2} \prod_{s=0}^{q-1} t_2 \omega^s (t_3 + t_1 \omega^s e^{-ik_1}) + \text{h.c.}) \\ &= -t_3^{2q} - t_1^{2q} - (t_3^q t_1^q (-1)^{q-1} e^{-iqk_1} + \text{h.c.}) - t_2^{2q} - (t_2^q t_3^q e^{ik_2} + t_2^q t_1^q (-1)^{q-1} e^{i(k_2 - qk_1)} + \text{h.c.}) \\ &= -|t_1^q e^{i((q-1)\pi - qk_1)} + t_2^q e^{-ik_2} + t_3^q|^2 \\ &= -\xi^2 \end{aligned} \quad (\text{S5})$$

Now we transform to another gauge $\mathbf{A}' = \hat{y}(x - \sqrt{3}y)B$, which extends the honeycomb unit cell in the \mathbf{a}_1 direction instead of \mathbf{a}_2 . Consequently, we have exchanged the momentum components k_1 and k_2 so that, now the only k_1 -dependent coefficient is a_0 . Therefore, we have proven that the only \mathbf{k} -dependent coefficient in (2a) is $a_0 = -\xi^2$. The momentum independent coefficients $a_n(\{t_i\})$, $n = 1, \dots, q$ can be determined recursively via Faddeev-LeVerrier algorithm. We present our results for $p = 1, q = 3, 4, 5$ as examples:

For $p/q = 1/3$:

$$\begin{aligned} a_1 &= 3(t_1^4 + t_2^4 + t_3^4 + t_2^2 t_3^2 + t_1^2 t_2^2 + t_1^2 t_3^2) \\ a_2 &= -3(t_1^2 + t_2^2 + t_3^2) \\ a_3 &= 1. \end{aligned} \tag{S6}$$

For $p/q = 1/4$:

$$\begin{aligned} a_1 &= (t_1^6 + t_2^6 + t_3^6) + t_1^4(t_2^2 + t_3^2) + t_2^4(t_1^2 + t_3^2) + t_3^4(t_1^2 + t_2^2) + 2t_1^2 t_2^2 t_3^2 \\ a_2 &= -6(t_1^4 + t_2^4 + t_3^4) - 8(t_1^2 t_2^2 + t_1^2 t_3^2 + t_2^2 t_3^2) \\ a_3 &= 4(t_1^2 + t_2^2 + t_3^2) \\ a_4 &= -1. \end{aligned} \tag{S7}$$

For $p/q = 1/5$:

$$\begin{aligned} a_1 &= 5(t_1^8 + t_2^8 + t_3^8) + 5(t_1^6(t_2^2 + t_3^2) + t_2^6(t_3^2 + t_1^2) + t_3^6(t_1^2 + t_2^2)) + 5(t_1^4 t_2^4 + t_2^4 t_3^4 + t_1^4 t_3^4) + \frac{15 + 5\sqrt{5}}{2} t_1^2 t_2^2 t_3^2 (t_1^2 + t_2^2 + t_3^2) \\ a_2 &= -10(t_1^6 + t_2^6 + t_3^6) - 15(t_1^4(t_2^2 + t_3^2) + t_2^4(t_1^2 + t_3^2) + t_3^4(t_1^2 + t_2^2)) - \frac{45 + 5\sqrt{5}}{2} t_1^2 t_2^2 t_3^2 \\ a_3 &= 10(t_1^4 + t_2^4 + t_3^4) + 15(t_1^2 t_2^2 + t_1^2 t_3^2 + t_2^2 t_3^2) \\ a_4 &= -5(t_1^2 + t_2^2 + t_3^2) \\ a_5 &= 1. \end{aligned} \tag{S8}$$

PROPERTIES OF THE THOULESS FUNCTION

In this section we provide more detailed analysis of the Thouless function and the constraints imposed upon the Chern bands. As discussed after in the main text, the mapping from the Thouless function $\xi(\{t_i\}, k_1, k_2)$ to the band energies $\{E_\alpha(\xi), \alpha = 1, \dots, 2q\}$ determines the position of the band extremal and saddle points of all bands for the system with arbitrary rational flux $\phi = \frac{p}{q}\phi_0$. We show in Fig.(S1) the extremal and saddle points of $\xi(\{t_i\}, k_1, k_2)$ for $q = 1$ in the two relevant hopping parameter regime $t_2 = t_3 = 1, t_1 < 2$ and $t_1 > 2$. The behavior of the energy bands $E_\alpha(\xi)$ for $q > 1$ can thus be similarly derived upon the appropriate replacement $(k_1, k_2) \rightarrow (qk_1 - \pi(q-1), k_2)$ and $\{t_i\} \rightarrow \{t_i^q\}$. Moreover, due to particle-hole symmetry, we are led to consider only the bands above charge-neutrality and define the band index $\beta \equiv \alpha - q$. Therefore, when $0 < t_1 < 2^{1/q}$, the band minimum (maximum) and maximum (minimum) for β odd (even) occur, respectively at $\xi(\mathbf{k}_{0\pm}^{(n)}) = \xi_{min} = 0$ and $\xi(\mathbf{k}_{max}^{(n)}) = \xi_{max} > 0$, where $\mathbf{k}_{0\pm}^{(n)} = ([\pm \arccos(-t_1^q/2) + \frac{\pi(2n+q-1)}{q}], \pm 2 \arccos(-t_1^q/2))$ and, furthermore, $\mathbf{k}_{max}^{(n)} = (\pi(2n+q-1)/q, 0)$. When $t_1 > 2^{1/q}$, $\xi(\mathbf{k}) > 0$ and the minimal of the β -odd bands and the maximal of the β -even bands are fixed in \mathbf{k} -space at the $\mathbf{M}_2^{(n)}$ points. We can further infer (i) that when $t_1 < 2^{\frac{1}{q}}$, the isolated energy bands satisfy $dE/d\xi = 0$ at $\xi_{min} = 0$ so as to prevent the discontinuity in $\nabla E(\mathbf{k}_{0\pm}^{(n)})$ and (ii) that the $t_1 < 2^{\frac{1}{q}}$ Chern transitions happen at $\xi(\mathbf{k}_{max}^{(n)}) = \xi_{max} = |2 + t_1^q|$, where $|dE/d\xi| \rightarrow \infty$ indicates the presence of q Dirac cones in the points $\mathbf{k}_{max}^{(n)}$ of the the magnetic Brillouin zone.

We now address an explanation on why transitions at $(\xi, E) = (0, E_F \neq 0)$ are forbidden in case (1) on the bottom of page 2. Let us begin by considering the band touchings at the particle-hole symmetric points $E = 0$. As discussed in the paragraph starting before Eq. (5), $E = 0$ band touchings occur whenever condition Eq. (6) is satisfied. So, as a consequence of particle-hole symmetry, there is an entire parameter regime where the two center bands touch at $E = 0$ forming $2q$ Dirac points localized at the zeros of ξ [the isotropic case was explicitly given in Eq. (5)]. To understand why $(\xi, E) = (0, E_F \neq 0)$ transitions do not occur, let us assume otherwise that two bands touch at such a point. Similarly to the steps discussed in the beginning of the section ‘‘IHC transitions’’ (page 2), the characteristic polynomial can be expressed as $\mathcal{P}(E) = c_2(E^2 - E_F^2)^2 - \xi^2 + O((E^2 - E_F^2)^4)$, leading to the relation in the vicinity of this hypothetical touching point:

$$E = \pm \alpha \xi, \quad \alpha = (4c_2 E_F^2)^{-1/2}, c_2 > 0.$$

So the assumed transition would have the same characteristics of the $2q$ Dirac touchings at $E = 0$. However, there is no particle-hole symmetry that protects these $E \neq 0$ transitions in parameter regime given by condition (6). Therefore, we find that the $(\xi, E) = (0, E_F \neq 0)$ transitions do not occur when condition (6) holds.

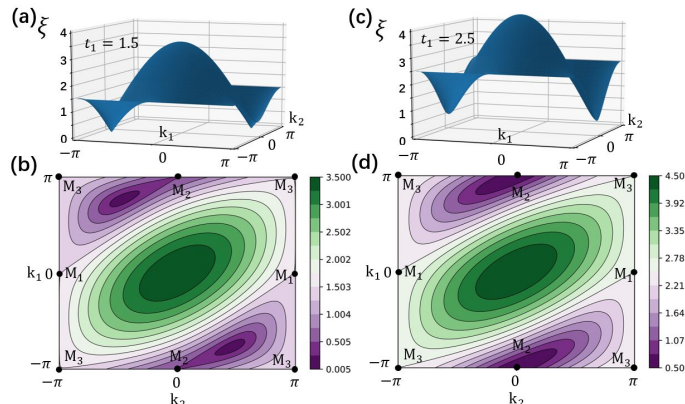


FIG. S1. (a) Thouless's function $\xi(\mathbf{k})$ with $q = 1$ (or equivalently $B = 0$) in the first Brillouin zone at $(t_1, t_2, t_3) = (1.5, 1, 1)$. (b) Contour plot of $\xi(\mathbf{k})$ with $q = 1$ at $(t_1, t_2, t_3) = (1.5, 1, 1)$. $\xi_{min} = 0$ at the Dirac points $\mathbf{k}_{0-} = -(\arccos(-0.75), 2 \arccos(-0.75)) = (-2.41, 1.44)$ and $\mathbf{k}_{0+} = (2.41, -1.44)$. (c) $\xi(\mathbf{k})$ with $q = 1$ in the first Brillouin zone at $(t_1, t_2, t_3) = (2.5, 1, 1)$. (d) Contour plot of $\xi(\mathbf{k})$ with $q = 1$ at $(t_1, t_2, t_3) = (2.5, 1, 1)$. $\xi_{min} > 0$ at $\mathbf{M}_2 = (-\pi, 0)$. The behavior for $q > 1$ follows upon replacing $(k_1, k_2) \rightarrow (q k_1 - \pi(q-1), k_2)$ and $\{t_i\} \rightarrow \{t_i^q\}$.

FURTHER EXAMPLES OF THE RELATION BETWEEN VHS AND CHERN TRANSITIONS

In this section we present more examples of the relationship between the VHS of the Dirac fermion band near charge neutrality of system A and the onset of topological phase transitions of system B, where the fluxes of A and B are close to each other. We first recall that the VHS of the $B = 0$ (alternatively, $q = 1$) graphene band splits into two when the hopping parameter t_1 is tuned away from the isotropic lattice $t_1 = t_2 = t_3 = 1$. These VHS energies above charge neutrality, $E_{VHS,1}$ and $E_{VHS,2}$, are given by

$$\begin{aligned} E_{VHS,1} &= E(\mathbf{M}_1) = E(\mathbf{M}_3) = |t_1|, \\ E_{VHS,2} &= E(\mathbf{M}_2) = |2 - t_1| \quad (t_1 < 2). \end{aligned} \quad (\text{S9})$$

If $t_1 > 2$, the Dirac points are gaped and $E_{VHS,2}$ disappears at the lower band edge. As an example, the DOS of the graphene band at different t_1 values is shown in Fig.(S2).

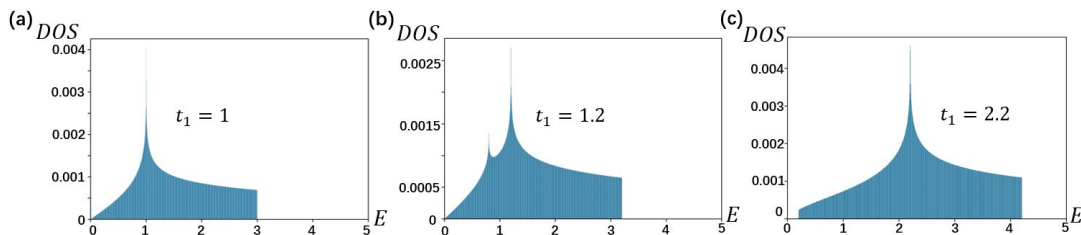


FIG. S2. (a) The $B = 0$ density of states at $(t_1, t_2, t_3) = (1, 1, 1)$. (b) The $B = 0$ density of states at $(t_1, t_2, t_3) = (1.2, 1, 1)$. The VHS split into two for $0 < t_1 < 2$. (c) The $B = 0$ density of states at $(t_1, t_2, t_3) = (2.2, 1, 1)$. The Dirac point is gaped and only $E_{VHS,1}$ is left.

The pattern of VHS splitting due to tuning the hopping parameters also persists to the Chern bands as a consequence of the implicit momentum dependence on Thouless function. In fact, the phenomenon associated with the VHS steering of Chern bands is observed either when $\phi_A = 0$ or when there is a nontrivial flux per unit cell. As argued in the main text, the following conditions must be satisfied: (a) For the steered system B (which undergoes Chern transitions) and the steering system A (which provides the “background” van Hove singularities), $[(\phi_B - \phi_A)/\phi_0] \ll 1$ and (b) $q_B \gg q_A$. We can understand the phase transitions of the system with $\phi_B = 1/q_B$ (with $q_B > 1$), in terms of the VHS of system

A in zero magnetic field. Below, we give concrete examples, one in Fig.(S3), which shows the Chern transitions of the $\phi_B = 1/7$ system and the second one in Fig.(S4), which corresponds to a composite fermion transition at $\phi_{CF} = 1/15$ and $n = 19/30$. In both cases, we see a clear relationship between the onset of phase transitions and the VHS of the $B = 0$ band. Furthermore, we point out that the VHS steering mechanism extends to some degree beyond the Dirac bands near charge neutrality discussed in the main text, as shown in Fig.(S5) for $\phi_A = 1/3$ and $\phi_B = 12/35$, albeit the mechanism for higher bands seems more sensitive to the narrow bandwidth of the Chern bands.

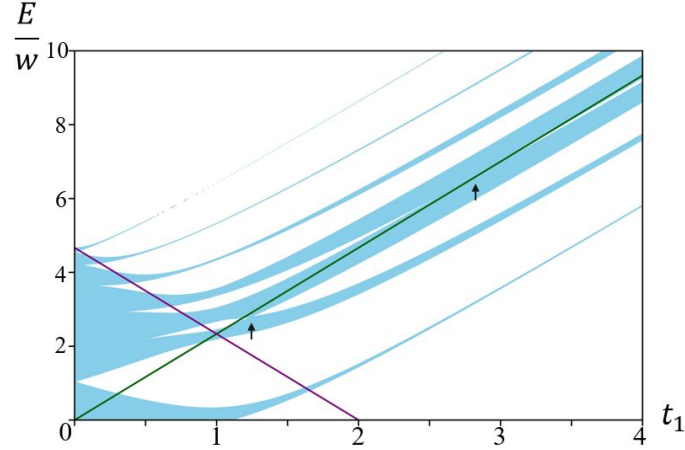


FIG. S3. $\phi = 1/7$ TPTs steered by the $B = 0$ VHS's. The green line shows the van Hove singularity $E_{\text{VHS},1}$ and the purple line showing $E_{\text{VHS},2}$. Here $w = 3/7$ is the average energy separation of bands of the $\phi = 1/7$ spectrum at $t_1 = t_2 = t_3 = 1$. The TPTs are pointed out with black arrows.

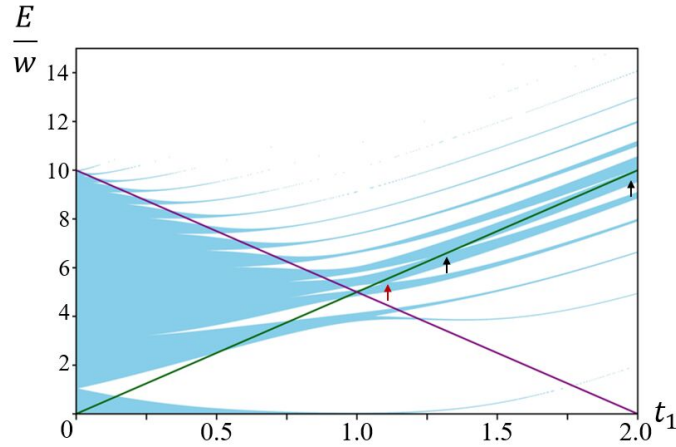


FIG. S4. $\phi_B = 1/15$ TPTs steered by the $B = 0$ VHS's. The green line shows the van Hove singularity $E_{\text{VHS},1}$ and the purple line showing $E_{\text{VHS},2}$. Here $w = 1/5$ is the average energy separation of bands of the $\phi = 1/15$ spectrum at $t_1 = t_2 = t_3 = 1$. The phase transitions are pointed out with vertical arrows, with the red arrow indicating the composite fermion phase transition.

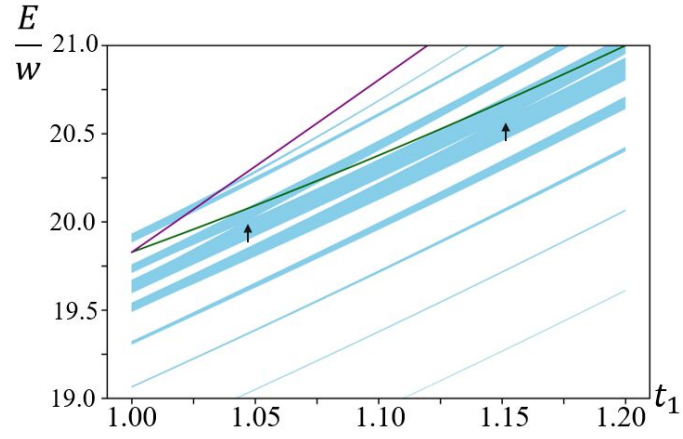


FIG. S5. $\phi_B = 12/35$ TPTs steered by the $\phi_A = 1/3$ VHS's of the 2nd band above charge neutrality as an example of the non-Dirac steering. The green line shows the van Hove singularity $E_{VHS,1}$ and the purple line showing $E_{VHS,2}$. Here $w = 3/35$ is the average energy separation of bands of the $\phi_B = 12/15$ spectrum at $t_1 = t_2 = t_3 = 1$. The TPT is pointed out with the black arrow. Notice that the band touchings deviates a little bit from $E_{VHS,1}$ suggesting a more complex mechanism behind the non-Dirac TPTs, presumably associated with a narrower band.